ISOMAse International Society of Ocean, Mechanical and Aerospace Scientists and Engineers

Journal of Ocean, Mechanical and Aerospace
-Science and Engineering-
30 March 2026. Vol.70 No.1

DOI:
10.36842/jomase.v70i1.571

Dynamic Response Analysis of Commuter Aircraft Windshield Under Drone Impact Using Finite Element Method

Noval Erlangga [a,*] and Raihan Farhan Ramadhan [b]

[a)] *Defense Industry, Republic of Indonesia Defense University, Indonesia*
[b)] *Aeronautical Engineering, Universitas Dirgantara Marsekal Suryadarma, Indonesia*

*Corresponding author: nvlairlangga@gmail.com

Paper History

Received: 24-November-2025
Received in revised form: 05-March-2026
Accepted: 30-March-2026

ABSTRACT

This study investigates the dynamic response of a commuter aircraft windshield subjected to drone impact and compares its damage characteristics with bird-strike conditions. Numerical simulations were conducted using the finite element method (FEM), incorporating variations in impact location, angle, and velocity. The results show that both impact location and angle significantly affect damage severity. For location and angle variations, the drone penetrated the windshield, with the most severe damage occurring at the center location and a 0° impact angle, resulting in maximum energy absorption of 1573.98 J. The plastic strain area at the center and at 0° was wider than at the upper edge and 22.5°, respectively. For velocity variations, the highest absorbed energy of 1975.04 J occurred at 105.5 m/s. At 58 m/s, cracking occurred without penetration, while penetration occurred at 80 m/s and above. Despite its lower mass compared to a 910 g bird, the drone impact proved more hazardous due to windshield penetration.

KEYWORDS: *Bird Strike, Drone, Finite Element Method, Unmanned Aerial Vehicle (UAV).*

NOMENCLATURE

CASR	Civil Aviation Safety Regulation
ECD	Viscoelastic Energy
EDC	Distortion Control Energy
EDMD	Failure Energy
EE	Elastic Strain Energy
EI	Internal Energy
EK	Kinetic Energy
EP	Plastic Strain Energy
FEM	Finite Element Method
SPH	Smoothed Particle Hydrodynamics
UAV	Unmanned Aerial Vehicle

1. INTRODUCTION

Foreign objects such as hail or bird strikes are highly susceptible to colliding with aircraft structures [1]. Civil aviation safety operations remain threatened by these impact incidents, which can lead to major accidents [2]. In recent years, collision threats to aircraft have evolved beyond natural objects to include human-made objects, notably unmanned aerial vehicles (UAVs), which operate in the same airspace as civil aviation. At present, the explosive growth of Unmanned Aircraft Vehicles (UAVs) has further complicated impact scenarios [3]. The global drone market is projected to reach approximately USD 73.06 billion in 2024, with sales volume reaching 10.3 million units in the consumer drone category. This reflects significant growth compared to the previous year, when the consumer market value stood at USD 12.1 billion in 2023 [4]. However, the rapid increase in UAV numbers has resulted in a higher frequency of accidents.

Although operational requirements for Small Unmanned Aircraft Systems have been regulated under Civil Aviation Safety Regulation (CASR) Part 107 [5], limited user education still contributes to potential collisions between drones and manned aircraft. Between 2010 and 2016, three collisions involving non-commercial aircraft occurred in Europe, including GBP 1,400 worth of damage to a Pioneer 300 in the UK, scratches on the wing surface of a French Robin DR400, and no structural damage when a Grumman AA-1 was struck on its undercarriage [6]. In 2020, an aircraft transporting the President of the United States was also reported to have nearly collided with a drone [7]. Furthermore, drone-impact airworthiness considerations have not yet been incorporated into existing aircraft design processes. This suggests that the likelihood of UAV–aircraft collisions exist, while the associated safety risks remain largely unknown. Therefore, evaluating collisions between UAVs and aircraft is considered necessary to minimize future damage [8].

JOMAse | Received: 24-November-2025 | Accepted: 30-March-2026 | [(70) 1: 1-12]
Published by International Society of Ocean, Mechanical and Aerospace Scientists and Engineers, www.isomase.org., ISSN: 2354-7065 & e-ISSN: 2527-6085

ISOMAse International Society of Ocean, Mechanical and Aerospace Scientists and Engineers
Journal of Ocean, Mechanical and Aerospace
-Science and Engineering-
30 March 2026. Vol.70 No.1
DOI: 10.36842/jomase.v70i1.571

Among aircraft structural components susceptible to external impacts, the windshield is considered particularly critical because its failure may directly compromise pilot safety and flight controllability [9].According to CASR Subpart 23.775, the windshield, directly in front of the pilot under normal operating conditions, and its supporting structure must be capable of withstanding (without penetration) the impact of a 2-pound (0.91 kg) bird at the aircraft's maximum flap-approach speed, relative to the bird along the flight path [10]. In the context of drone impacts, CASR Subpart 23.775 is referenced by equating the drone mass with that of a bird (0.91 kg) during a windshield impact event. Thus, a DJI Mavic drone with a mass of 735 g was selected as the projectile, and the windshield of a commuter-category aircraft was used as the target specimen [11].

This study aims to analyze the dynamic response of an aircraft windshield subjected to drone impact under variations of impact parameters (velocity, angle, and location) and to compare the resulting damage with that caused by bird strikes. Through this approach, the structural capability of the windshield to withstand drone impact loads can be assessed, and the differences in damage between drone impact and bird strike can be identified. The analysis is conducted numerically using the finite element method.

2. METHOD

The Finite Element Method (FEM) is employed in this study as a numerical approach to analyze the structural response resulting from high-velocity impact events between a UAV and an aircraft windshield. FEM enables detailed modeling of mechanical material behavior by discretizing continuous structures into finite elements, allowing stresses, strains, deformations, and damage responses to be evaluated comprehensively [12]. In this study, the FEM-based analysis involves material modeling and mass distribution, geometric design, and numerical simulation setup to realistically represent the impact conditions. The overall modeling and simulation process is conducted to accurately capture the dynamic interaction between the UAV and the windshield, thereby providing a reliable basis for assessing structural response characteristics and their implications for structural integrity and safety.

2.1 Materials and Mass Distribution

Aluminium 6061-T6 was selected as one of the primary materials in the drone structure due to its excellent combination of strength, ductility, and manufacturability [13]. This alloy is well known for its high strength-to-weight ratio, making it ideal for structural components such as drone frames or arms that require sufficient stiffness while remaining lightweight. In addition, aluminium 6061-T6 exhibits stable mechanical behaviour under dynamic loading, including high-velocity impact conditions, which makes it a commonly used material in commercial and small-scale industrial UAVs [14].

Polycarbonate (PC) is an engineering polymer widely used for protective drone components such as body shells, camera housings, and outer frame covers due to its high impact toughness, optical clarity, and thermoformability [15]. This material possesses excellent crack resistance and strong energy-absorption capability during impact, which is why it is often applied to components that are likely to undergo large deformations [16].

Lithium-ion cells serve as the primary power source for drones and contribute significantly to the total projectile mass in impact simulations. Beyond functioning as energy storage units, lithium-ion batteries exhibit complex mechanical and thermal characteristics, particularly when subjected to penetration or severe deformation during impact. Under impact loading, the internal cell structure may be damaged, potentially triggering heat release or even thermal runaway, thus increasing the hazard level associated with drone impacts [17].

Glass-epoxy (a fiberglass-reinforced epoxy composite) is commonly used in lightweight structural drone components such as landing gear supports, arm guards, or composite panels because it offers high specific strength, corrosion resistance, and a favourable response under dynamic loading [18]. This composite material exhibits typical damage modes such as delamination, matrix cracking, and fiber breakage when exposed to high-velocity impacts [19]. Its complex damage behaviour is particularly relevant for drone-impact simulations due to its distinct fragmentation characteristics and energy-dissipation mechanisms compared to metals. Studies on composite materials demonstrate that glass-epoxy may experience substantial reductions in strength after impact, making accurate modelling in finite element essential for representing the impact phenomenon realistically.

Windshields of commuter aircraft generally use Polymethyl Methacrylate (PMMA) or acrylic due to their optical clarity, lightweight characteristics, and ability to be formed into curved panels [20]. However, PMMA possesses lower impact toughness compared to polycarbonate and tends to exhibit brittle behavior under high-velocity impacts, making it susceptible to cracking, shattering, or even penetration when subjected to collisions with hard objects such as drones [21].

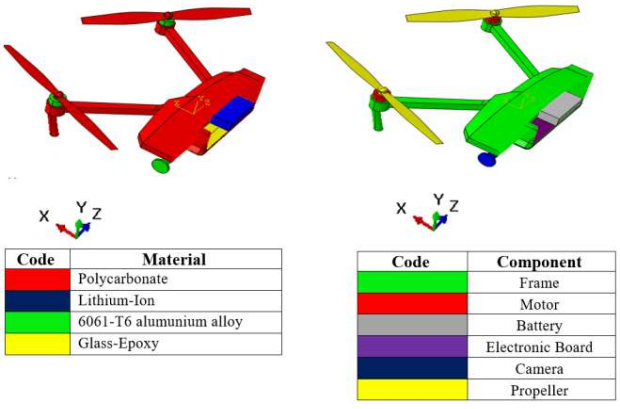

Figure 1: Drone material properties

Table 1: Drone mass distribution

Component	Mass (g)
Frame	544
Motor	24.2
Battery	35.7
Electronic Board	31.6
Camera	13.1
Propeller	86.7
Total	753.3

JOMAse | Received: 24-November-2025 | Accepted: 30-March-2026 | [(70) 1: 1-12]
Published by International Society of Ocean, Mechanical and Aerospace Scientists and Engineers, www.isomase.org., ISSN: 2354-7065 & e-ISSN: 2527-6085

ISOMAse
International Society of Ocean, Mechanical and Aerospace Scientists and Engineers
Journal of Ocean, Mechanical and Aerospace
-Science and Engineering-
30 March 2026. Vol.70 No.1
DOI:
10.36842/jomase.v70i1.571

2.2 Geometry Design

The drone model used in this study has the geometry comparable to the "Mavic" series supplied by DJI, as illustrated in Figure 2. The drone dimensions are 220 × 275 × 83 mm, with a total mass (including the camera) of 735 g. This mass closely approximates the bird mass required in airframe bird-strike certification, which is 910 g. Several geometric features and minor components were omitted in the modeling process; however, their masses were incorporated into the primary structure to ensure that the total mass and center of gravity remained unchanged. In the model, the frame, propellers, and electronic board were represented using shell elements, whereas the battery, camera, and motors were modeled using solid elements.

The geometry of the windshield is shown in Figure 3, modeled using 3D deformable elements. The windshield was assigned a thickness of 9 mm and serves as the impact target, with a total mass of 3.84 kg. One of the commonly used simulation techniques for bird-strike analysis is the Smoothed Particle Hydrodynamics (SPH) method. This method was developed to overcome mesh distortion issues encountered in high-velocity impact problems [22]. In SPH-based bird modeling, the bird's body is represented as a soft material that behaves similarly to a viscoplastic fluid when subjected to high-speed impact.

In this approach, the bird is represented as a collection of mesh-free particles that interact with one another through a kernel function, enabling the model to capture extreme deformation, fragmentation, and material flow—phenomena that cannot be effectively handled using conventional finite element methods.

The SPH method provides a more realistic prediction of peak impact pressure and force distribution patterns because it can accurately capture the breakup dynamics of the bird's body as well as the transfer of impulsive energy to the target structure. Studies also show that the choice of constitutive model significantly influences the simulation outcome, with viscoplastic models offering the best agreement with the physical phenomena observed in actual bird-strike events [23].

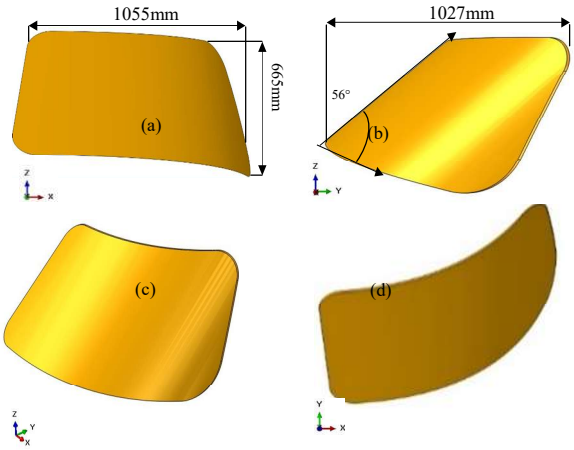

Figure 3: Geometry of windshield; (a) Front view, (b) Side view, (c) Isometric view, (d) Top view [27]

2.3 Simulation Setup

2.3.1 Assembly

The impact angle between the drone model and the windshield was varied at 0° and –22.5°, while the bird model and windshield were simulated at an impact angle of 0°, as shown in Figures 4 and 5. Location 1 was selected to evaluate downward deformation (perpendicular to the aircraft's longitudinal axis). Significant deformation in this direction may pose a risk to the pilot's head. This location was chosen because it represents the area farthest from the supporting structure and is directly positioned in front of the pilot during operational tasks.

2.3.2 Meshing

The meshed drone model is shown in Figure 7. The drone model consists of 4,935 shell elements and 2,409 solid elements. Each component contains a different number of elements, as presented in Table 2.

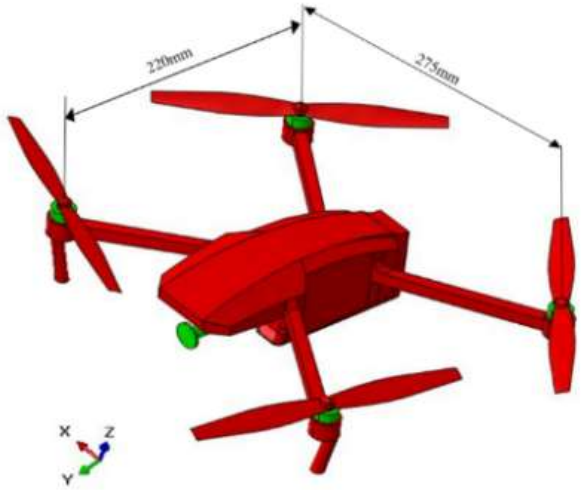

Figure 2: Model of drone geometry

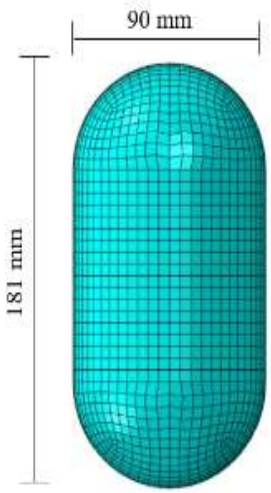

Figure 4: Bird model geometry

JOMAse | Received: 24-November-2025 | Accepted: 30-March-2026 | [(70) 1: 1-12]
Published by International Society of Ocean, Mechanical and Aerospace Scientists and Engineers, www.isomase.org., ISSN: 2354-7065 & e-ISSN: 2527-6085

ISOMAse International Society of Ocean, Mechanical and Aerospace Scientists and Engineers
Journal of Ocean, Mechanical and Aerospace
-Science and Engineering-
30 March 2026. Vol.70 No.1
DOI: 10.36842/jomase.v70i1.571

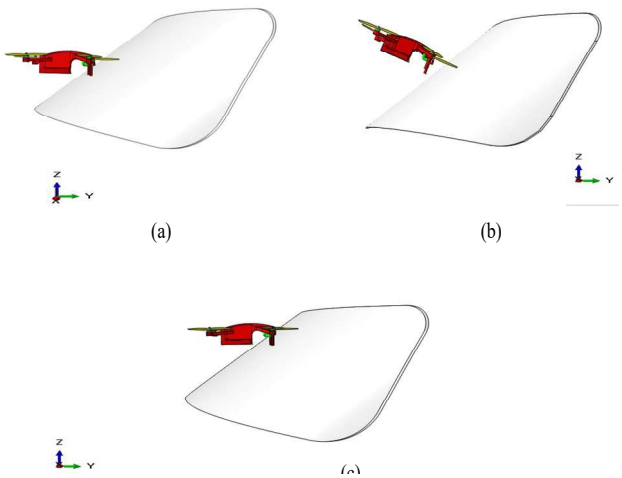

Figure 5: Assembly of the drone and windshield model: (a) location 2 at an impact angle of 0°, (b) location 2 at an impact angle of –22.5°, and (c) location 1 at an impact angle of 0°

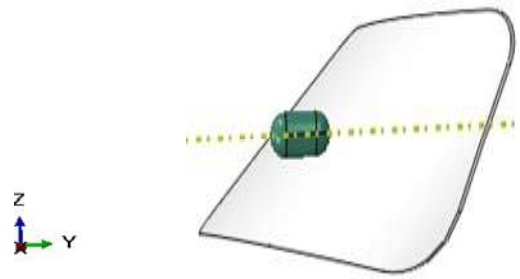

Figure 6: Assembly of the bird model and windshield at location 2 with an impact angle of 0°

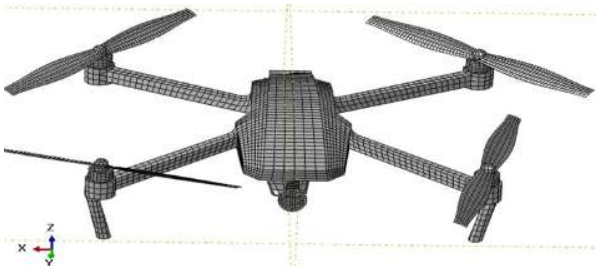

Figure 7: Meshing of the UAV model

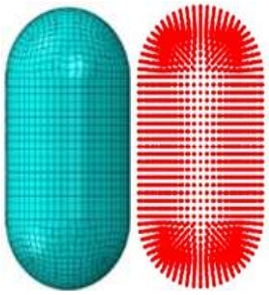

Figure 8: SPH particle discretization of the bird model

Table 2: Number of mesh elements of drone

Mesh Element	Component	Number of Elements
5mm	Battery	165
5mm	Motor	744
5mm	Frame	4005
5mm	Propeller	744
5mm	Electronic Board	186
2mm	Camera	1500

Figure 9: Finite element meshing of the windshield model

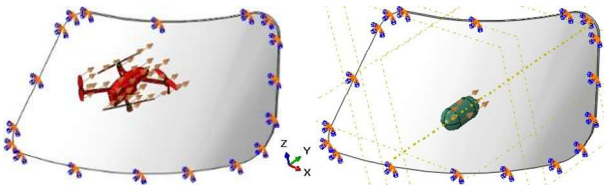

Figure10: Loading and boundary conditions on the windshield model for: (a) the drone, (b) the bird

For the bird model, the number of elements depends on the L/D ratio. The mesh is then converted into a set of particles, as is characteristic of the SPH method. The SPH bird model consists of 11,797 particles, as shown in Figure 8.

It should be noted that this bird model is homogeneous and does not account for anatomical differences such as muscle or bone; therefore, it can only be used to predict the macro-level structural response in bird-strike simulations. The meshed windshield model, consisting of 16,144 elements, is shown in Figure 9.

2.3.3 Interaction

The contact type employed is General Contact (Explicit) as it represents the entire model for analysis. The friction behavior between the drone and the windshield is defined with a coefficient of 0.26 [24]. For the bird, a critical damping fraction of 0.4 is applied to reduce the magnitude of pressure during the initial phase of the steady state [25].

2.3.4 Load and Boundary Condition

In this study, the boundary conditions for the dynamic impact response analysis are defined in three main categories; constraint boundary conditions, initial conditions, and contact conditions. Constraint boundary conditions are applied at the edges of the windshield by restraining translational and rotational displacements along the x-, y-, and z-axes to

JOMAse | Received: 24-November-2025 | Accepted: 30-March-2026 | [(70) 1: 1-12]
Published by International Society of Ocean, Mechanical and Aerospace Scientists and Engineers, www.isomase.org., ISSN: 2354-7065 & e-ISSN: 2527-6085

represent the windshield being supported by the surrounding edge-supporting structure. Initial conditions are applied to the drone and bird models in the form of prescribed initial velocities, which serve as the loading parameters to initiate the impact event, such that the initial kinetic energy becomes the primary source of the system's dynamic response. Furthermore, contact conditions are defined to model the nonlinear interaction between the impacting objects and the windshield during the impact event, allowing realistic force transfer and deformation while preventing non-physical numerical penetration [26].

Velocity is the loading parameter applied to the drone and bird models (indicated by arrows in Figure 10). Boundary conditions are applied at the edges of the windshield, as shown in Figure 10. This is considered because the windshield is supported by the edge-supporting structure, which restrains translational and rotational displacements along the x, y, and z axes.

3. RESULT

3.1 Simulation Based on Location Variation

Simulation variations were conducted to study the effect of different impact locations on the dynamic response of the windshield and to determine the most critical scenario for windshield damage. The impact velocity used for the location simulations was 80 m/s. This impact velocity is a relative value, consisting of the drone's maximum speed of 18 m/s and the aircraft's speed of 62 m/s at maximum flap approach. The aircraft speed was chosen in accordance with aviation regulations for bird strikes, specifically CASR 23.775. Two impact locations were analyzed: Location 1 (upper edge of the windshield) and Location 2 (center of the windshield). Simulations were conducted with the impact velocity and angle as fixed variables, namely 80 m/s and 0°.

In Figure11, the areas marked with arrows indicate stress concentrations, which are considered the initial failure locations. Stress at Location 1 occurs at the upper edge, while Location 2 experiences stress at the center of the windshield. If the stress exceeds the material's yield strength of 68 MPa, plastic deformation occurs; and if it approaches the maximum material stress of 78 MPa, failure will ensue.

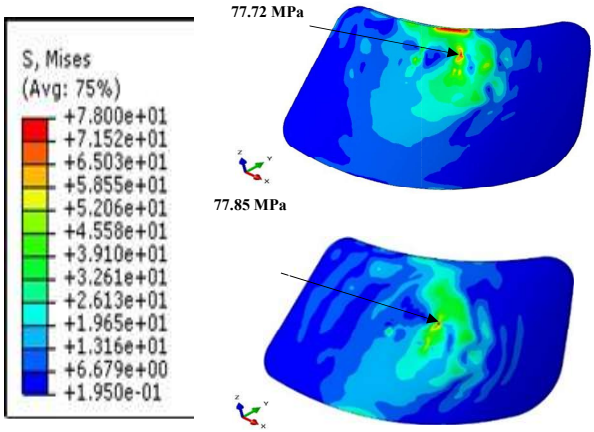

Figure 11: Stress distribution on windshield for location variations

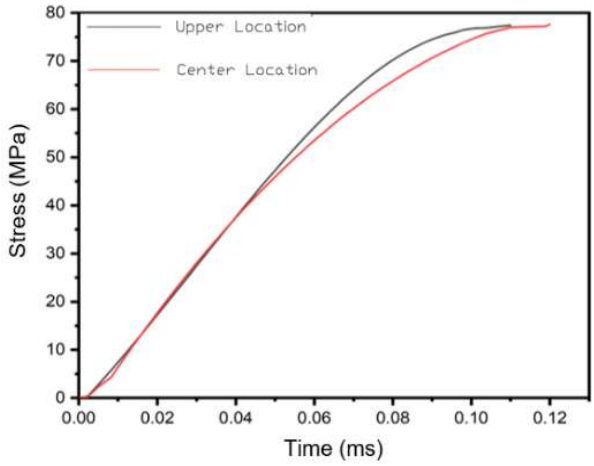

Figure 12: Stress on the windshield for location variations over the time interval: (a) Location 1; (b) Location 2

Based on Figure 12, locations 1 and 2 experienced failures, with their respective maximum stresses of 77.72 MPa and 77.85 MPa at 0.11 ms and 0.12 ms. Plastic strain at Location 1 occurs at the upper edge of the windshield, indicating that this area experiences stress exceeding the material's yield strength. The displacements at Locations 1 and 2 are presented in Figure 13, with maximum displacements of 35.40 mm and 24.50 mm, respectively.

The windshield begins to develop initial cracking (local failure) at the upper region, which is considered the critical factor, and the crack propagates along the y- and z-axis vectors, leading to global failure of the windshield as shown in Figure 14. The drone penetrates the upper edge of the windshield.

At Location 2, plastic strain occurs at the center of the windshield. The windshield develops initial cracking (local failure) at the central region, and the crack propagates along the y- and z-axis vectors, resulting in global failure of the windshield as shown in Figure 14. This occurs because Locations 1 and 2 exhibit maximum strain values that exceed the material's maximum failure criterion, which is 0.067.

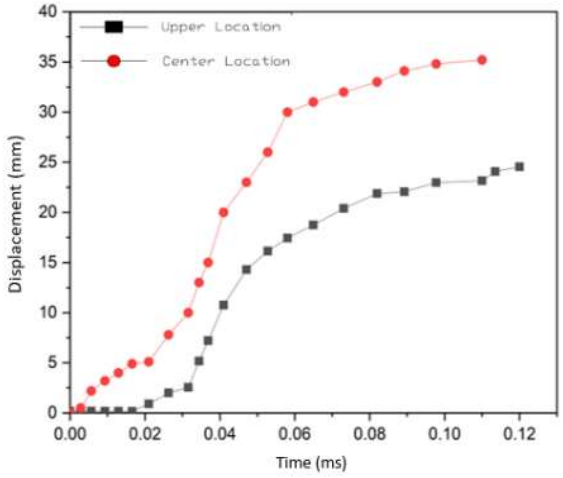

Figure 13: Displacement of the windshield over time at Locations 1 and 2

JOMAse | Received: 24-November-2025 | Accepted: 30-March-2026 | [(70) 1: 1-12]
Published by International Society of Ocean, Mechanical and Aerospace Scientists and Engineers, www.isomase.org., ISSN: 2354-7065 & e-ISSN: 2527-6085

ISOMAse
International Society of Ocean, Mechanical and Aerospace Scientists and Engineers
Journal of Ocean, Mechanical and Aerospace
-Science and Engineering-
30 March 2026. Vol.70 No.1
DOI:
10.36842/jomase.v70i1.571

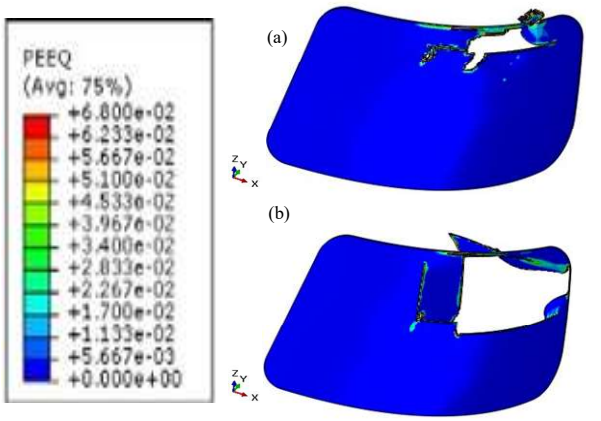

Figure 14: Plastic strain regions on the windshield for location variations: (a) Location 1; (b) Location 2

Overall, the kinetic and internal energy curves exhibit similar patterns for each impact location variation. However, the maximum values of each energy component differ at each location [27]. The internal energy (EI) is the sum of the elastic strain energy (EE), plastic strain energy (EP), viscoelastic energy (ECD), failure energy ($EDMD$), and distortion control energy (EDC), which can be expressed as follows:

$$E_I = E_E + E_P + E_{CD} + E_{DMD} + E_{DC} \quad (1)$$

In general, the energy involved in an impact event is the kinetic energy, which is calculated using the following equation:

$$E_K = \frac{1}{2} m u_0^2 \quad (2)$$

At the onset of impact, a decrease in the drone's kinetic energy and an increase in the windshield's internal energy occur at both locations. The reduction in the drone's kinetic energy is caused by the impact (contact) between the drone and the windshield, which results in a decrease in both the drone's velocity and mass. The increase in internal energy at both locations is attributed to elastic and plastic deformation.

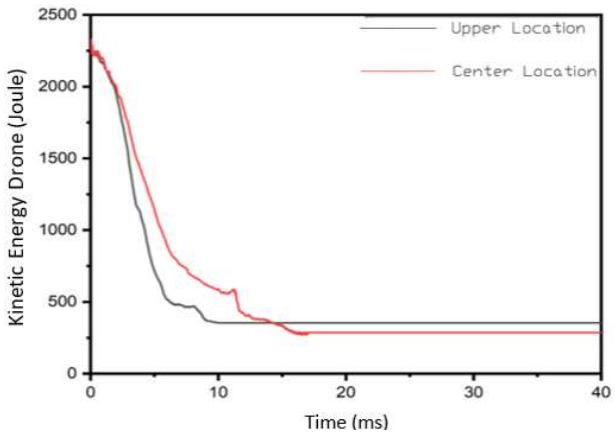

Figure 15: Drone kinetic energy at Locations 1 and 2

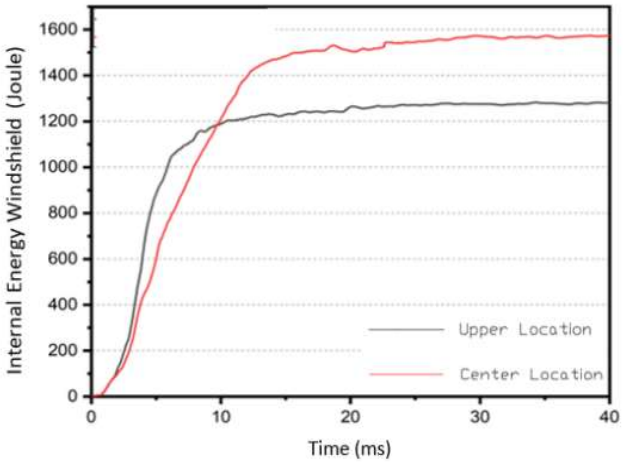

Figure 16: Windshield internal energy at Locations 1 and 2

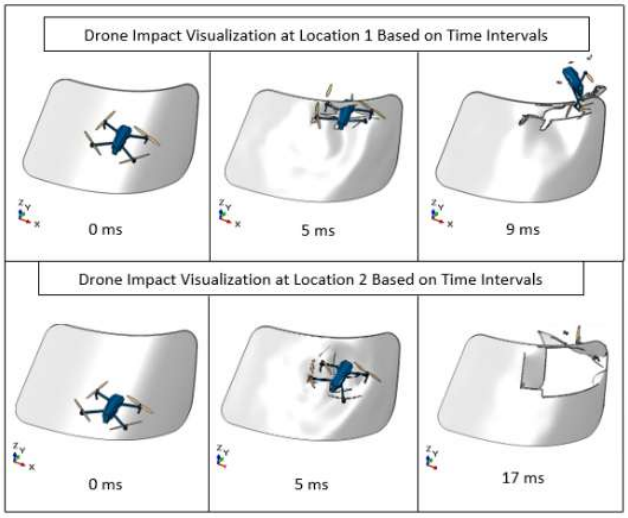

Figure 17: Simulation of drone impact at an impact velocity of 80 m/s and an angle of 0°,based on location variations: (a) Location 1; (b) Location 2

In Figure 15, the drone's kinetic energy of 2274 J at both locations is absorbed by the deformation of the windshield and subsequently decreases to a constant value of approximately354 J at Location 1 and 286 J at Location 2 at 0.9 ms and 17 ms, respectively, when the drone penetrates the windshield with reduced velocity and mass.

Figure 16 presents the internal energy at Locations 1 and 2 for an impact velocity of 80 m/s and an angle of 0°, with a drone mass of 735 grams. At both locations, the internal energy curves tend to increase due to significant deformation of the windshield, with maximum absorbed internal energy values of 1283.92 J and 1573.98 J for Locations 1 and 2, respectively. As time progresses, the internal energy curves at both locations stabilize because the drone has already penetrated the windshield, resulting in no further energy absorption. Location 2 experiences more severe damage than Location 1 because it is situated farther from the support (edge of the windshield).

JOMAse | Received: 24-November-2025 | Accepted: 30-March-2026 | [(70) 1: 1-12]
Published by International Society of Ocean, Mechanical and Aerospace Scientists and Engineers, www.isomase.org., ISSN: 2354-7065 & e-ISSN: 2527-6085

ISOMAse
International Society of Ocean, Mechanical and Aerospace Scientists and Engineers
Journal of Ocean, Mechanical and Aerospace
-Science and Engineering-
30 March 2026. Vol.70 No.1
DOI:
10.36842/jomase.v70i1.571

Figure 17 shows that the drone's kinetic energy is progressively absorbed by the windshield through structural deformation during impact at both locations. At the initial contact stage, localized bending and indentation occur at the impact area, marking the onset of energy transfer from the drone to the windshield. As the deformation increases, stresses redistribute around the impact zone, and the drone's velocity decreases due to kinetic energy dissipation. When the material resistance is exceeded, progressive damage develops, including crack initiation, crack propagation, large deflection, and eventual perforation. Although the overall response pattern is similar at both locations, differences in deformation magnitude and penetration time are observed due to variations in local structural behavior and stress distribution.

3.2 Simulation Based on Impact Angle Variations

Simulation variations were conducted to examine the influence of different impact angles on the dynamic response of the windshield and to determine the most critical scenario for windshield damage. The impact velocity used for the angular variation simulations was 80 m/s. Based on the Location Variation Simulation, Location 2 experienced the most severe damage; therefore, Location 2 was selected as the impact point for this analysis. Two impact angles were analyzed: 0° and –22.5°. The simulations were performed with a constant impact velocity of 80 m/s, fixed at Location 2.

Figure 18 presents the stress distribution visualization for the 0° and –22.5° impact angles. In Figure 18, the areas marked with arrows indicate stress concentrations, which are considered the initial failure locations.

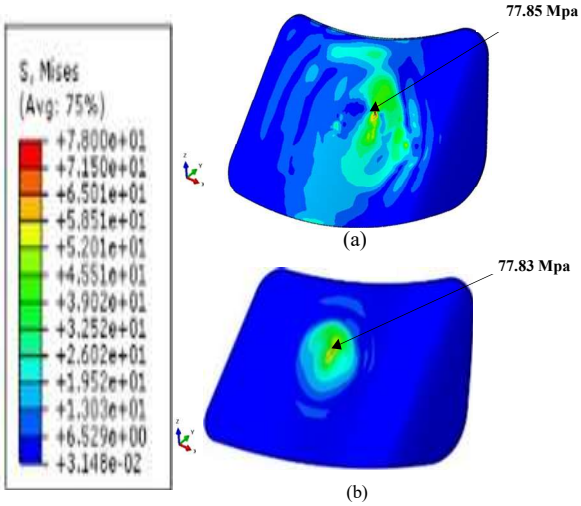

Figure 18: Stress distribution on windshield for impact angle variations: (a) 0°, (b) –22.5°

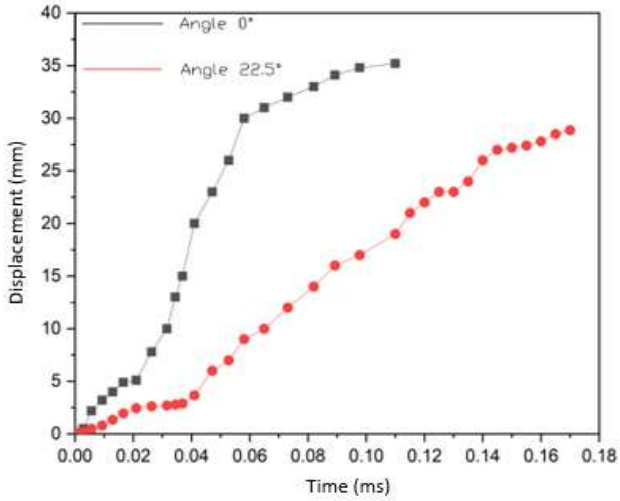

Figure 20: Displacement of the windshield over time at 0° and –22.5°

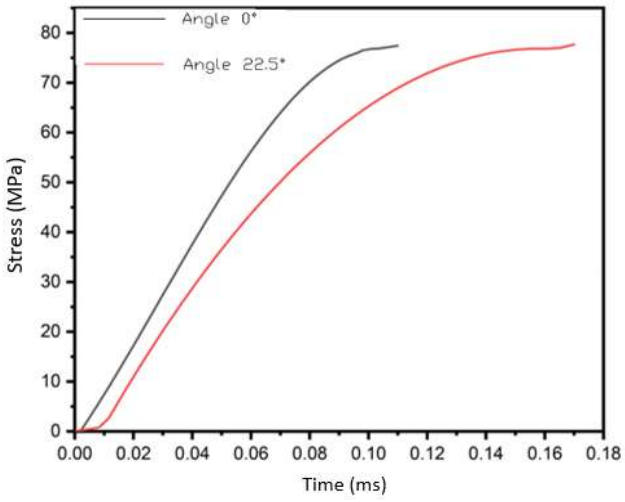

Figure 19: Stress on the windshield for impact angle variations over time

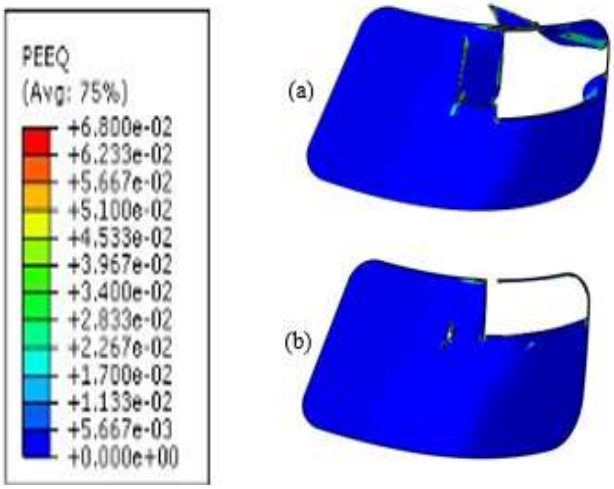

Figure 21: Plastic strain regions on the windshield for impact angle variations: (a) 0°, (b) –22.5°

JOMAse | Received: 24-November-2025 | Accepted: 30-March-2026 | [(70) 1: 1-12]
Published by International Society of Ocean, Mechanical and Aerospace Scientists and Engineers, www.isomase.org., ISSN: 2354-7065 & e-ISSN: 2527-6085

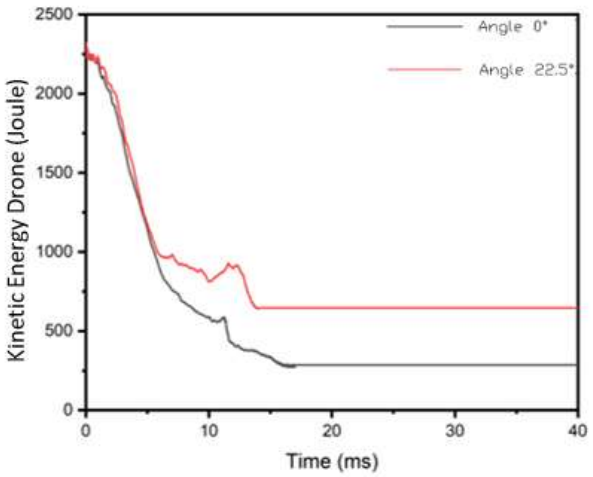

Figure 22: Drone kinetic energy for impact angle variations

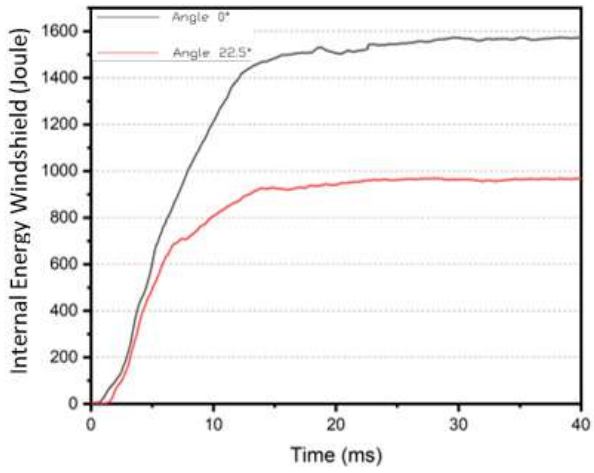

Figure 23: Windshield internal energy for impact angle variations

Based on Figure 19, the maximum stresses for the 0° and –22.5° impact angles are 77.85 MPa and 77.83 MPa at 0.10 ms and 0.17 ms, respectively. The stresses for both angles exceed the material's yield strength of 68 MPa and are nearly equal to the ultimate material stress of 78 MPa. The displacements for the 0° and –22.5° impact angles are shown in Figure 20. The maximum displacements for each angle are 35.40 mm and 28.90 mm, respectively.

The plastic strain region expands as the impact angle becomes more normal, as shown in Figure 21. For both angles, plastic strain occurs from the middle to the upper region of the windshield, indicating that these areas experience stresses exceeding the yield strength. The windshield begins to develop initial cracking (local failure) at the central region, which is considered the critical factor. The crack propagates along the y- and z-axis vectors, resulting in global failure, as illustrated in Figure 21. Both angles experience initial cracking followed by crack propagation and eventual global failure because their maximum strain values exceed the material's failure strain criterion of 0.067.

In Figure 22, the drone's initial kinetic energy of 2274 J at both angles is absorbed by windshield deformation and subsequently decreases to a constant value of approximately 286 J at 0° and 978 J at –22.5° at 17 ms and 0.7 ms, respectively, when the drone penetrates the windshield with reduced velocity and mass.

As shown in Figure 23, a more normal impact angle results in greater energy absorption by the windshield. Failure occurs at both angles (0° and –22.5°). For both angles, the energy curves tend to increase after the onset of failure due to large deformation in other windshield elements, with absorbed internal energies of 1573.98 J and 968.94 J, respectively. As time progresses, the internal energy curves stabilize because the drone has fully penetrated the windshield.

3.3 Simulation Based on Velocity Variation

The impact velocity was varied to determine the severity of damage to the windshield when a 735 g drone collides with it. Three different velocities were investigated based on the following considerations. First, according to reference [23], drones are not permitted to operate above 400 ft (approximately 120 m). Second, the maximum allowable flight altitude for the drone is limited to 500 m above ground level by DJI. Reference [24] states that, unless authorized by the Administrator, no person may operate an aircraft below 10,000 ft (approximately 3,000 m) MSL at an indicated airspeed greater than 250 knots (129 m/s). Therefore, three aircraft velocities were selected based on the flight envelope: 40 m/s during take-off (approximately 120 m), 62 m/s during approach (approximately 500 m), and 87.5 m/s during cruising (approximately 5000 m). With the drone's maximum flight speed of 18 m/s, the resulting impact velocities were 58 m/s, 80 m/s, and 105.5 m/s. The simulation was conducted at Location 2 with an impact angle of 0°.

Figure 25 shows the stress distribution, where the regions marked with arrows indicate stress concentrations that represent the initial failure locations.

Based on Figure 26, the maximum stresses at velocities of 58, 80, and 105.5 m/s are 77.71 MPa, 77.85 MPa, and 77.76 MPa at 0.17 ms, 0.12 ms, and 0.78 ms, respectively. The stresses at all velocity variations exceed the material's yield strength of 68 MPa and are nearly equal to the ultimate strength of 78 MPa. In Figure 27, the largest maximum displacement occurs at 105.5 m/s, with a value of 42.90 mm, while the smallest displacement occurs at 58 m/s, with a value of 28.80 mm.

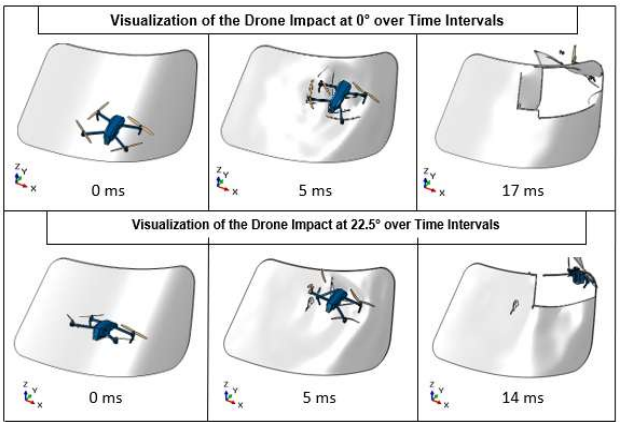

Figure 24: Numerical simulation of drone impact on the windshield at different impact angles

JOMAse | Received: 24-November-2025 | Accepted: 30-March-2026 | [(70) 1: 1-12]
Published by International Society of Ocean, Mechanical and Aerospace Scientists and Engineers, www.isomase.org., ISSN: 2354-7065 & e-ISSN: 2527-6085

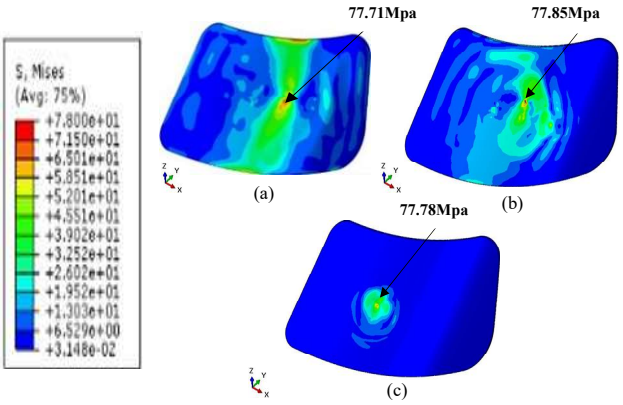

Figure 25: Stress distribution on the windshield for different impact velocities: (a) 58 m/s, (b) 80 m/s, (c) 105.5 m/s

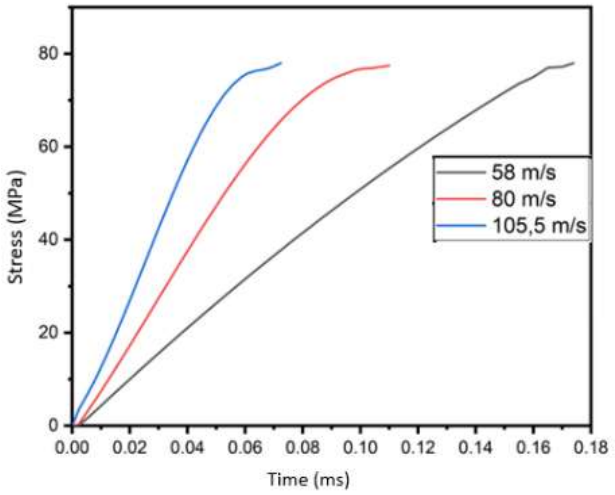

Figure 26: Stress on the windshield for different impact velocities

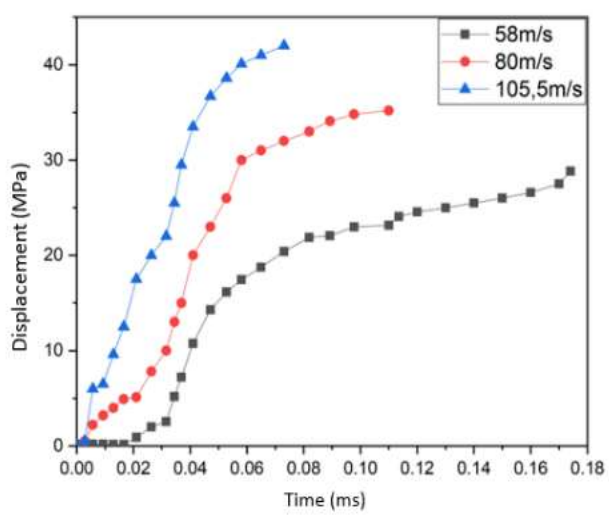

Figure 27: Displacement on the windshield for different impact velocities

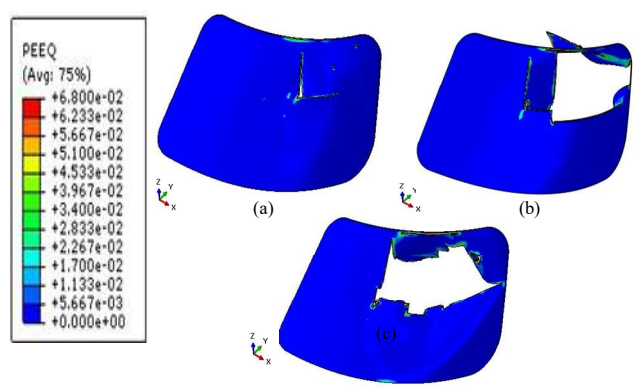

Figure 28: Plastic strain area on the windshield for velocity variations: (a) 58 m/s; (b) 80 m/s; (c) 105.5 m/s

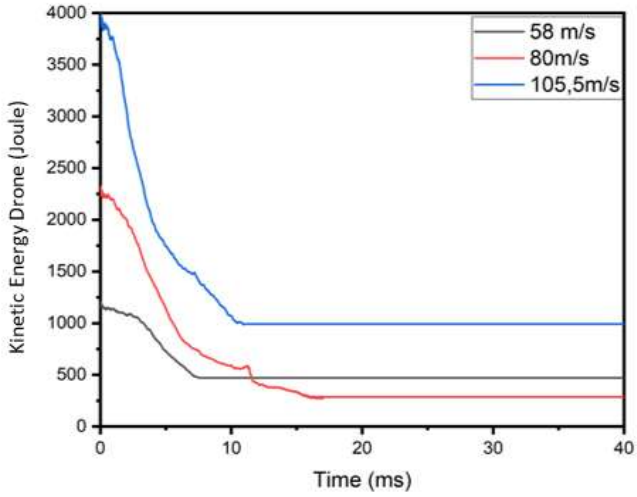

Figure 29: Drone kinetic energy at different velocities

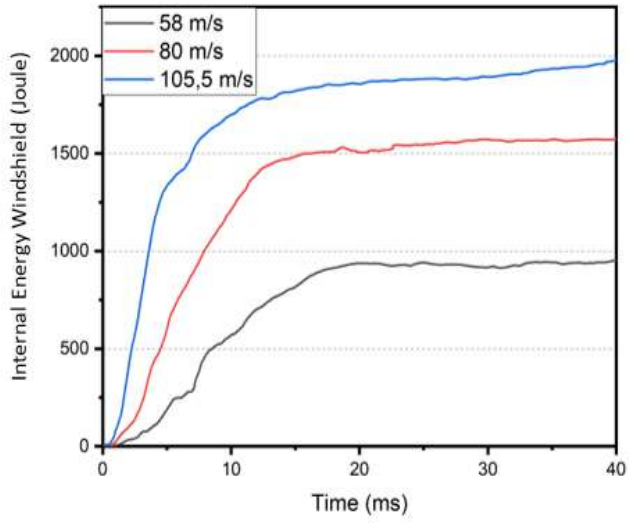

Figure 30: Windshield internal energy at different velocities

JOMAse | Received: 24-November-2025 | Accepted: 30-March-2026 | [(70) 1: 1-12]
Published by International Society of Ocean, Mechanical and Aerospace Scientists and Engineers, www.isomase.org., ISSN: 2354-7065 & e-ISSN: 2527-6085

ISOMAse
International Society of Ocean, Mechanical and Aerospace Scientists and Engineers
Journal of Ocean, Mechanical and Aerospace
-Science and Engineering-
30 March 2026. Vol.70 No.1
DOI:
10.36842/jomase.v70i1.571

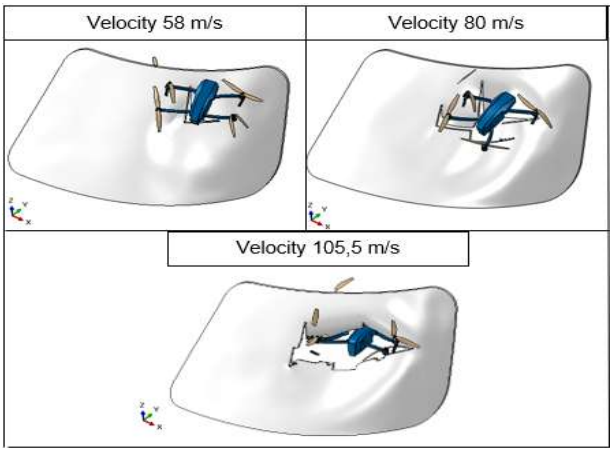

Figure 31: Simulation of drone impact at an impact angle of 0° at Location 2 for different velocities

The plastic strain area expands as the impact velocity increases, as shown in Figure 28. Failure occurs in the middle to upper part of the windshield, indicating that this area experiences stress exceeding the yield strength of the material. The windshield begins to experience an initial crack (local failure) in the central region, which is considered the critical factor, and the cracking propagates in the direction of the *y* and *z* axis vectors, leading to global failure of the windshield as shown in Figure 28.

The windshield experiences an initial crack (local failure) in the central region, and the cracking propagates in the direction of the *y* and *z* axis vectors, resulting in global failure. Since all three velocities (58 m/s, 80 m/s, and 105.5 m/s) have maximum strain values that exceed the maximum failure criterion of the material, which is 0.067, the windshield undergoes failure.

In Figure 29, the drone's kinetic energy at the three impact velocities (58, 80, and 105.5 m/s), namely 1158 J, 2274 J, and 3908 J, is absorbed by the deformation of the windshield and subsequently decreases to a constant value at each velocity: approximately 471 J for 58 m/s, 286 J for 80 m/s, and 991 J for 105.5 m/s, at 17 ms and 0.7 ms respectively, when the drone penetrates the windshield accompanied by reductions in its speed and mass.

Based on Figure 30, an increase in impact velocity results in a greater amount of energy absorbed by the windshield. At the velocity variations (58, 80, and 105.5 m/s), the energy curves tend to rise after reaching the onset of failure due to significant deformation occurring in other elements of the windshield, with maximum internal energy absorption values of 951.22, 1573.98, and 1975.04 Joules, respectively. As time progresses, the internal energy curves of the windshield tend to stabilize because the drone has already penetrated the windshield.

3.4 Comparison of Drone Impact and Bird Strike

The bird strike simulation on the windshield was conducted using the same numerical framework as that employed for the drone impact analysis. All modeling procedures, including the definition of windshield geometry, specification of boundary conditions, assignment of initial impact velocity, and configuration of impact angle, were implemented consistently across both scenarios.

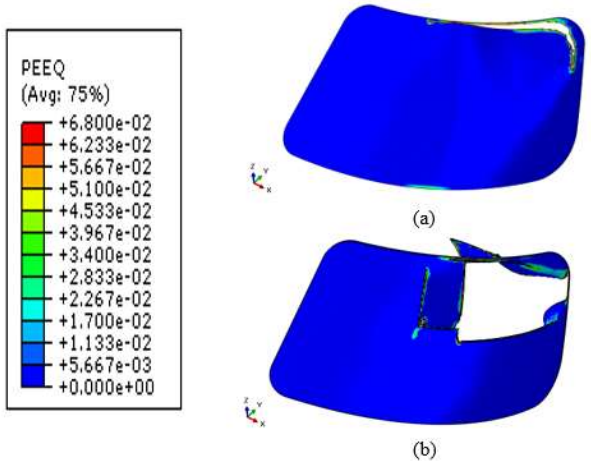

Figure 32: Plastic strain area on the windshield for: (a) bird strike, (b) drone impact

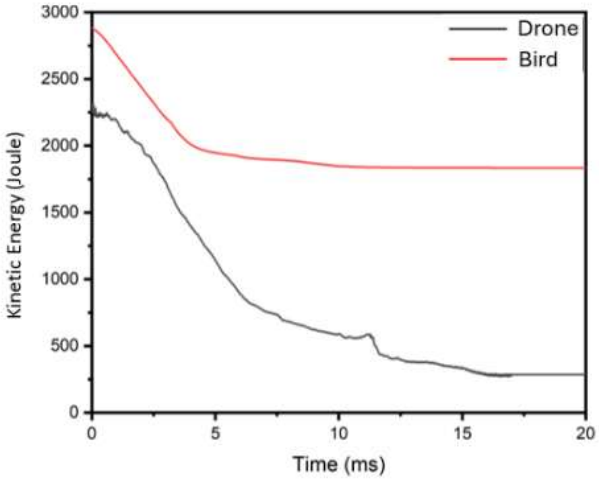

Figure 33: Comparison of kinetic energy of the bird and the drone

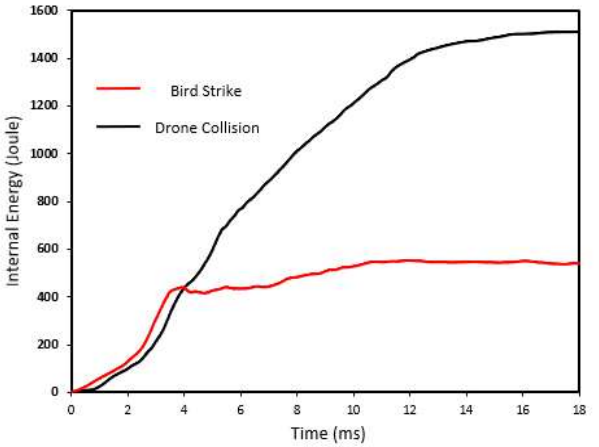

Figure 34: Internal energy of the windshield during drone impact and bird strike

JOMAse | Received: 24-November-2025 | Accepted: 30-March-2026 | [(70) 1: 1-12]
Published by International Society of Ocean, Mechanical and Aerospace Scientists and Engineers, www.isomase.org., ISSN: 2354-7065 & e-ISSN: 2527-6085

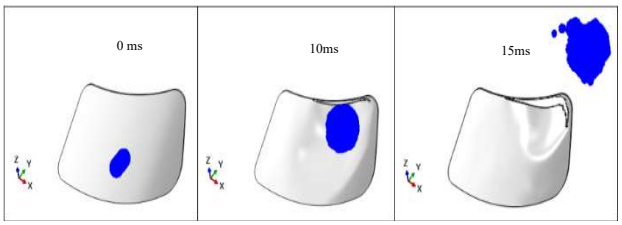

Figure 35: Numerical simulation of bird impact on the windshield

During the bird-strike event, damage occurs at the upper edge of the windshield, whereas during the drone-impact event, the windshield experiences severe damage in the central region because the drone penetrates the windshield, resulting in a wider plastic strain area compared to the bird strike.

The comparison between the 735 g drone impact and the 910 g bird strike is shown in Figure 32. In both cases, the impact velocity is set to 80 m/s, and the impact is applied at Location 2, corresponding to the central region of the windshield, with an impact angle of 0°. These identical impact parameters are selected to ensure a consistent basis for comparison, allowing the differences in plastic strain distribution and damage patterns to be attributed primarily to the distinct physical characteristics of the impacting objects rather than variations in loading conditions.

In Figure 33, the comparison of the drone's kinetic energy with that of the bird is presented, showing that the bird leaves the windshield earlier and the energy transfer from the bird to the windshield is smaller than that of the drone.

The energy absorption is shown in Figure 34, indicating that the windshield absorbs more energy during the drone impact than during the bird strike, meaning that larger deformation occurs in the drone-impact scenario. The maximum absorbed energy in the bird strike and the drone impact is 553.30 and 1573.98 Joules, respectively.

4. CONCLUSION

For the impact location variations (upper edge and centre) and impact angle variations of 0° and 22.5°, the drone penetrated the windshield, resulting in severe damage. The highest energy absorption occurred at the centre location and at the 0° angle, with a value of 1573.98 J. In the location variation, the plastic strain area at the centre was wider than at the upper edge, indicating more severe damage at the centre. In the angle variation, the plastic strain area at 0° was wider than at 22.5°, indicating that the 0° impact caused more severe damage. For the impact velocity variation (58, 80, and 105.5 m/s), the highest energy absorption occurred at 105.5 m/s, with a value of 1975.04 J. At 58 m/s, the drone did not penetrate the windshield but caused cracking at the centre region. At 80 m/s and 105.5 m/s, the drone penetrated the windshield, resulting in severe structural damage. The drone impact on the in-flight windshield, despite having a lower mass (735 g) than the bird (910 g), is more dangerous because the drone penetrates the windshield, which can expose the pilot and co-pilot to potentially fatal injuries.

REFERENCES

[1] Ashmi, G. V. & Priyadharsini, R. (2024). The modern approaches for identifying foreign object debris (fod) in aviation. In *2024 International Conference on Integrated Circuits and Communication Systems (ICICACS)* (pp. 1-5). IEEE.

[2] Taupik, J., Alamsyah, T., Wulandari, A., Armin, E.U., & Hikmaturokhman, A. (2023). Airport runway foreign object debris (fod) detection based on yolox architecture. *2023 International Conference on Computer Science, Information Technology and Engineering (ICCoSITE)*, 40-43.

[3] Uzuntaş, K.N. & Aslan, M. (2025). Unmanned aerial vehicles and aviation safety: a qualitative study. *The Aeronautical Journal*, *129*(1340), 2919–2937. doi:10.1017/aer.2025.10038.

[4] Grand View Research (2025). Drone Market (2025-2030). https://www.grandviewresearch.com/industry-analysis/drone-market-report.

[5] Directorate General of Civil Aviation. (2020). *Civil Aviation Safety Regulation (CASR) Part 107: Small Unmanned Aircraft Systems*. Ministry of Transportation, Republic of Indonesia.

[6] European Aviation Safety Agency. (2016). *UAS Safety Risk Portfolio and Analysis (Safety Intelligence and Performance SM1.1)*. Cologne, Germany: EASA.

[7] Charpentreau, C. (2023). Air Force One possibly involved in near-miss incident with drone - AeroTime. AeroTime. https://www.aerotime.aero/articles/25669-air-force-one-possibly-involved-in-near-miss-incident-with-drone.

[8] Mukhlis, A.H. (2021). *Penguatan Pengaturan Pesawat Udara Tanpa Awak (Drone) Melalui Undang-Undang*. IBLAM Law Review, 1(2), 103–120.

[9] Rezaei, M., Arezoo, B., &Ziaei-Rad, S. (2024). Redesign an aircraft windshield to improve its mechanical resistance against simultaneous bird impacts. *International Journal of Impact Engineering*, *184*, 104811.

[10] Directorate General of Civil Aviation. (2014). *Civil Aviation Safety Regulation (CASR) Part 23, Amendment 2: Airworthiness Standards-Normal, Utility, Acrobatic, and Commuter Category Airplanes*. Ministry of Transportation, Republic of Indonesia.

[11] Mavic Pro - Product Information - DJI. DJI Official. https://www.dji.com/id/mavic/info.

[12] Harsch, J. & Eugster, S.R. (2020). Finite Element Analysis of Planar Nonlinear Classical Beam Theories

[13] Sarif, M.I., Ramli, M.F., & Mohd Saleh, S.J. (2023). Weight Reduction of C-Drone Body Structure. *Progress in Aerospace and Aviation Technology*.

[14] Hong, T., Ding, F., Chen, F., Zhang, H., Zeng, Q. & Wang, J. (2023). Mechanical properties of 6061 aluminum alloy under cyclic tensile loading. *Crystals*, *13*(8), 1171.

[15] Ghavanini, N., Caporale, A.M., Astori, P., Airoldi, A. & Panichelli, P. (2023). Impact Response of Monolithic and Laminated Polycarbonate Panels: An Experimental and Numerical Investigation. *Polymers, 15*.

[16] Seif, A., Mahmoud, S.F. & Megahed, M. (2024). Enhancement of Impact, Shear and Wear Performance of Glass Fiber/Epoxy Composites by Inclusion of Polycarbonate Sheets. *Fibers and Polymers, 25*, 4421 - 4436.

[17] Wang, G., Guo, X., Chen, J., Han, P., Su, Q., Guo, M., Wang, B. & Song, H. (2023). Safety Performance and Failure Criteria of Lithium-Ion Batteries under Mechanical Abuse. *Energies*.

[18] Al-Shamary, A.K., Abed, A.R. & Karakuzu, R. (2023). A comparative study on ballistic impact behaviors of glass/epoxy composites. *Mechanics of Advanced Materials and Structures, 31*, 13341 - 13350.

[19] Anuse, V.S., Shankar, K., Velmurugan, R. & Ha, S.K. (2023). Compression-after-impact analysis of carbon/epoxy and glass/epoxy hybrid composite laminate with different ply orientation sequences. Thin-Walled Structures, 185, 110608.

[20] Edo, G.I., Ndudi, W., Ali, A.B., Yousif, E., Zainulabdeen, K., Onyibe, P.N., Akpoghelie, P.O., Ekokotu, H.A., Isoje, E.F., Igbuku, U.A., Essaghah, A.E., Ahmed, D.S. & Umar, H. (2024). An updated review on the modifications, recycling, polymerization, and applications of polymethyl methacrylate (PMMA). *Journal of Materials Science, 59*, 20496 - 20539.

[21] Rasan, D. & Farhan, F.A. (2023). Effect of addition of polymerized polymethyl methacrylate (PMMA) and zirconia particles on impact strength, surface hardness, and roughness of heat cure PMMA: An in vitro study. *Dental Hypotheses, 14*, 36 - 38.

[22] Shao, J., Xie, H., Liu, N., Yang, Y. & Zheng, Z. (2023). An improved composite impact damage model and bird-striking damage analysis with smoothed particle hydrodynamics-finite element method. *Journal of Reinforced Plastics and Composites, 43*, 939 - 958.

[23] Kwon, S.L., Kim, S., Kim, K. & Yun, G.J. (2023). Birdstrike Analysis of the Flap Driving Parts Considering Effects of Bird Geometry and SPH(Smoothed Particle Hydrodynamics) Parameters. *Journal of the Korean Society for Aeronautical & Space Sciences*.

[24] Lu, X., Liu, X., Li, Y., Zhang, Y. & Zuo, H. (2020). Simulations of airborne collisions between drones and an aircraft windshield. *Aerospace Science and Technology*, *98*, 105713.

[25] Pavlović, A. & Minak, G. (2023). FEM-SPH numerical simulation of impact loading on floating laminates. *Journal of Marine Science and Engineering*, *11*(8), 1590.

[26] Federal Aviation Administration. (2020). *14 CFR Part 107 – Small Unmanned Aircraft Systems*. U.S. Department of Transportation.

[27] Warsiyanto, B.A., Sitompul, S.A., Yuniarti, E., Fitriansyah, R. & Utama, A.B. (2020). Bird strike analysis on 19 passenger aircraft windshield with different thickness and impact velocity. *Jurnal Teknologi Kedirgantaraan*, *5*(2).

JOMAse | Received: 24-November-2025 | Accepted: 30-March-2026 | [(70) 1: 1-12]
Published by International Society of Ocean, Mechanical and Aerospace Scientists and Engineers, www.isomase.org., ISSN: 2354-7065 & e-ISSN: 2527-6085